

The Plerionic Supernova Remnant G21.5-0.9: In and Out

Heather Matheson and Samar Safi-Harb

*Department of Physics and Astronomy, University of Manitoba, Winnipeg,
Manitoba, R3T 2N2, CANADA matheson@physics.umanitoba.ca,
samar@physics.umanitoba.ca*

Advances in Space Research, in press

Abstract

The absence of a supernova remnant (SNR) shell surrounding the Crab and other plerions (pulsar wind nebulae) has been a mystery for 3 decades. G21.5-0.9 is a particularly intriguing plerionic SNR in which the central powering engine is not yet detected. Early *CHANDRA* observations revealed a faint extended X-ray halo which was suggested to be associated with the SNR shell; however its spectrum was nonthermal, unlike what is expected from an SNR shell. On the other hand, a plerionic origin to the halo is problematic since the X-ray plerion would be larger than the radio plerion. We present here our analysis of an integrated 245 ksec of archival *CHANDRA* data acquired with the High-Resolution Camera (HRC) and 520 ksec acquired with the Advanced CCD Imaging Spectrometer (ACIS). This study provides the deepest and highest resolution images obtained to date. The resulting images reveal for the first time 1) a limb-brightened morphology in the eastern section of the halo, and 2) a rich structure in the inner ($40''$ -radius) bright plerion including wisps and a double-lobed morphology with an axis of symmetry running in the northwest-southeast direction. Our spatially resolved spectroscopic study of the ACIS-I data indicates that the photon index steepens with increasing distance from the central point source out to a radius of $40''$ then becomes constant at ~ 2.4 in the X-ray halo (for a column density $N_H = 2.2 \times 10^{22} \text{ cm}^{-2}$). No line emission was found from the eastern limb; however marginal evidence for line emission in the halo's northern knots was found. This study illustrates the need for deep *CHANDRA* observations to reveal the missing SNR material in Crab-like plerions.

Key words: ISM: individual (G21.5-0.9), Stars: Neutron, ISM: Supernova Remnants, X-Rays: ISM

1 Introduction

G21.5-0.9 has been classified as a plerionic SNR since it has a flat radio spectrum, centrally peaked radio and X-ray emission, and a highly polarized radio flux (Green, 2004). At a distance of ~ 5 kpc the $80''$ -diameter plerion would have a linear size of ~ 2 pc.

Prior to *XMM* and *CHANDRA* observations there was no evidence for a central energy source in G21.5-0.9 and the X-ray and radio distributions were similar. *CHANDRA* observations in 1999 revealed a faint X-ray halo ($\sim 150''$ radius) and showed that the central bright ($40''$ -radius) plerion was surrounding a $2''$ compact centre (Slane et al., 2000; Safi-Harb et al., 2001). The spectrum of G21.5-0.9 was described by a powerlaw with the photon index increasing with distance from the central source. No evidence of thermal emission from the halo was found using 6 *CHANDRA* ACIS-S observations (Safi-Harb et al., 2001). Early *XMM* observations also showed that the halo has a nonthermal spectrum (Warwick et al., 2001). A plerionic origin to the halo is problematic because of the larger X-ray size when compared to the radio size, and a shock-heated supernova material origin is also problematic because of the absence of limb-brightening and thermal emission. While the nature of the halo is unclear, it was suggested that it could be partially caused by dust scattering since G21.5-0.9 is a bright and heavily absorbed source (Safi-Harb et al., 2001).

The X-ray halo was later modelled using *XMM* data as a dust-scattering halo. It was found that the halo could not be due to dust-scattering alone. As well, a thermal component was detected in the northern knots (whose presence cannot be explained by the dust model), but not elsewhere in the halo (Bandiera and Bocchino, 2004).

G21.5-0.9 was chosen as a calibration target for the *CHANDRA* X-ray observatory and, as a result there are numerous observations publicly available. Here, we concentrate on imaging with the Advanced CCD Imaging Spectrometer (ACIS) and the High-Resolution Camera (HRC), as well as a spectral analysis of the -120°C ACIS-I data.

2 Imaging

Images were created from observations taken between 1999 Aug. 23 and 2004 Mar. 26 with ACIS, and between 1999 Sept. 4 and 2003 May 17 with HRC-I. All data processing was performed with the software package CIAO 2.3. Each observation was processed individually to create a cleaned event file by retaining events with ASCA grades 02346 and rejecting hot pixels. As well, the data was filtered for good time intervals, removing periods with high background rates or unstable aspect. The observations were combined using the CIAO tools *reproject_events* and *dmmerge*. A summary of the exposure times for the *CHANDRA* observations is given in Table 1. The maximum and minimum off-axis angles for the ACIS data were $9.3'$ (observation 1441) and $0.3'$

(observations 159 and 1230), respectively. The total integrated exposure times for the ACIS images and HRC-I images were 520.3 ksec (194.6 ksec with off-axis angle $< 2'$) and 245.2 ksec (all observations had off-axis angle $< 0.4'$), respectively. This is more than a magnitude deeper than previous studies.

2.1 *The Halo*

Using 59 ACIS observations (269.7 ksec with ACIS-I and 250.6 ksec with ACIS-S), we created images of G21.5-0.9 in the soft (red, 0.2-1.5 keV), medium (green, 1.5-3.0 keV), and hard (blue, 3.0-10.0 keV) energy bands (smoothed with a Gaussian distribution, $\sigma = 2.5''$). The soft energy image reveals the X-ray halo as incomplete in the southwest, whereas the medium energy image shows a nearly circular halo. The X-ray halo is least evident in the hard image. The images of the three energy bands were then combined to form the colour image in Fig. 1. Limb-brightening is observed for the first time at the boundary of the X-ray halo, most noticeably in the medium energy band and on the eastern side. Radial profiles (Fig. 4) were created of the southeast and southwest quadrants, yielding the level of limb-brightening.

In Fig. 2, we show the corresponding intensity image (520.3 ksec integrated exposure time). The left image spans the entire remnant ($377''$, smoothed with $\sigma = 2.5''$), while the right image spans the central $94''$ (smoothed with $\sigma = 1''$) and highlights the structure observed in the plerion. Again, the eastern limb is visible. This shell-like structure indicates that we have likely detected the SNR shell. Most notably in the halo is a knotty structure visible in the northern part of the halo (also referred to in previous work as the northern spur). This region is of particular interest as it has a radio counterpart (B. Gaensler, private communication). In §3, we present its spectrum which suggests that it could be due to enhanced emission from swept-up supernova material.

2.2 *High-Resolution Imaging of the Inner Plerion*

The bottom panel of Fig. 1 and the right panel of Fig. 2 show the ACIS energy color image (as in §2.1) and the false-colour image of the inner bright component ($40''$ -radius). The HRC-I image (245.2 ksec exposure, 13 observations) is shown in Fig. 3.

The compact source is clearly visible at the centre of the plerion, and filamentary structures are noticeable features of the plerion in all images. In particular, the high-resolution HRC image reveals wisp-like features south-east of the compact source near $\alpha=18^h33^m34.0^s$ and $\delta=-10^\circ34'10.5''$ (J2000), and northwest of the compact source near $\alpha=18^h33^m33.3^s$ and $\delta=-10^\circ33'58.0''$ (J2000). Similar features have been observed in known pulsar wind nebulae and are believed to result from the deposition of the pulsar wind's energy into its surroundings.

Furthermore, our deep images confirm the double-lobed morphology of the plerion previously seen in the earlier images (Safi-Harb et al., 2001). This

structure is particularly visible in the northwest, as indicated by the line of symmetry running from northwest to southeast. The indentation in the northwest of the X-ray emission is correlated with a trough in the radio, supporting the picture that the symmetric lobes could be evidence of pulsar jets (Fürst et al., 1988). Modelling of the plerion is beyond the scope of this paper and will be addressed in future work.

3 Spectral Analysis

The ACIS-I, -120°C data (Table 1) was filtered for good time intervals and ASCA grades 02346, yielding 127.5 ksec of data used in the spectral analysis. A CTI correction was performed on each observation using the CIAO tool *acis_process_events*.

The regions selected for analysis were the bright knots in the north of the SNR and the limb-brightening observed in the east (Fig. 2), as well as concentric rings of increasing radius centred on the compact central source (5'' increments from 0'' to 45'', 10'' increments from 45'' to 165''). Note that the bright plerion extends to 40'', the brightest knots in the north of the remnant are located at 70''-95'', and the limb-brightening in the southeast of the remnant is observed at 120''-150''.

The spectra were grouped using *grppha* to a minimum 100 counts per bin for the northern knots and a minimum 50 counts per bin for the eastern limb. The 15 spectra for a particular region were fit simultaneously using XSPEC. The command *group* was used in XSPEC to produce a plot with spectra from all ACIS-I, -120°C observations combined (§3.2 and §3.3).

3.1 Plerion and Extended Emission

Spectra obtained from concentric rings, centered on the compact center at $\alpha = 18^h33^m33^s$ and $\delta = -10^\circ34'08''$ (J2000), were fit with a powerlaw (with N_H allowed to vary, and with $N_H = 2.2 \times 10^{22} \text{ cm}^{-2}$, which was the column density found by fitting a powerlaw to the remnant, consistent with Safi-Harb et al. (2001)). We found that the photon index, Γ , increases with radius from 1.61 ± 0.04 (1.43 ± 0.02 with $N_H = 2.2 \times 10^{22} \text{ cm}^{-2}$) at 0'' – 5'' to 2.15 ± 0.13 (2.13 ± 0.06 with $N_H = 2.2 \times 10^{22} \text{ cm}^{-2}$) at the edge of the plerion (Fig. 5, errors are 90% confidence). When N_H is allowed to vary, the general trend is a decrease in N_H with an increase in radius (Fig. 5). Above 40'' the number of counts decreases dramatically, but Γ seems to be constant at ~ 2.4 ($N_H = 2.2 \times 10^{22} \text{ cm}^{-2}$). The constant value for the photon index across the halo suggests that the halo is unlikely to be an extension of the plerion (see §3.2 and §3.3). No evidence for thermal emission was found within a radius of 40''.

3.2 Northern Bright Knots

The spectrum of the bright knots in the north of the remnant shows marginal evidence of line emission. Fitting a powerlaw to this region (Fig. 6, resulted in a photon index of $\Gamma = 2.07 \pm 0.14$ ($N_H = 1.86 \pm 0.20 \times 10^{22} \text{ cm}^{-2}$) with a reduced χ^2 of 1.11 (dof=108). Excess emission is visible near 1.84 keV, 2.38 keV, 2.64 keV indicating the presence of silicon and sulfur in the knots. Adding gaussians on top of the powerlaw at 1.84 keV, 2.38 keV and 2.64 keV produced F-test probabilities of 0.845, 5.4×10^{-3} , and 3.3×10^{-3} respectively, indicating that the addition of the gaussians significantly improves the fit.

The XSPEC *ps shock* model was then used to search for thermal emission that may be due to shock-heated ejecta or interstellar matter. As shown in Table 2, the *ps shock* model provides an adequate fit; however with a lower column density, an unrealistically high temperature and a low ionization timescale. Fitting a two component model (powerlaw+*ps shock*) to the bright knots, a good fit is also obtained with $N_H = 2.46 (2.04-3.15) \times 10^{22} \text{ cm}^{-2}$ (which is consistent with N_H towards the central plerion), a photon index of 2.33 (2.12-2.57) and $kT = 0.14 (0.08-0.20) \text{ keV}$ (reduced $\chi^2 = 1.08$, dof=105). Additional *CHANDRA* data will help constrain the thermal component parameters (see also Bocchino, these proceedings, for an *XMM* study of this region).

3.3 Eastern Outermost Arc

In Table 2, we summarize the spectral fitting results to the limb-brightened region in the east of the remnant; and in Fig. 7 we show the powerlaw fit. No line emission is observed in this region. However, due to the low count rate, the inclusion of additional observations may reveal additional detail in the spectrum.

4 Conclusions

Deep *CHANDRA* imaging of G21.5-0.9 reveals previously unseen detail, in both the plerion and the X-ray halo. Limb-brightening is revealed in the eastern portion of the X-ray halo, and wisp-like structures reminiscent of shocked pulsar winds are observed in the plerion. A spectral analysis performed with ACIS-I data shows the plerion is fit well by a powerlaw with a photon index that increases with radius from the centre of the plerion. However, the photon index is constant across the X-ray halo, indicating that the halo is unlikely an extension of the plerion. Marginal evidence was found for line emission in the bright knots in the north of the SNR, suggesting the presence of swept-up supernova material. Future work includes a spectral analysis of all ACIS-S data in addition to the ACIS-I data, which could reveal additional detail in the spectra; a timing analysis of all the available observations, a correlation of the X-ray data with the observations at radio and infrared

wavelengths, and modeling of our results.

The authors acknowledge support by the Natural Sciences and Engineering Research Council (NSERC) of Canada. H. Matheson is an NSERC PGS-M fellow and S. Safi-Harb is an NSERC University Faculty Award fellow.

We thank the referees for their useful comments.

References

- Bandiera, R., Bocchino, F. The X-ray halo of G21.5-0.9. *Adv. Space Res.* 33, 398-402, 2004.
- Fürst, E., Handa, T., Morita, K. et al. Detection of axisymmetric filaments in the filled-center supernova remnant G21.5-0.9. *Publ. Astron. Soc. Japan.* 40, 347-356, 1988.
- Green, D. A. A Catalogue of Galactic Supernova Remnants. Mullard Radio Astronomy Observatory, Cavendish Laboratory, Cambridge, 2004.
- Safi-Harb, S., Harrus, I.M., Petre, R. et al. X-ray observations of the supernova remnant G21.5-0.9. *Astrophys. J.* 561, 308-321, 2001.
- Slane, P., Chen, Y., Schulz, N.S. et al. Chandra observations of the Crab-like supernova remnant G21.5-0.9. *Astrophys. J.* 533, L29-L32, 2000.
- Warwick, R.S., Bernard, J-P., Bocchino, F. et al. The extended X-ray halo of the Crab-like SNR G21.5-0.9. *Astron. Astrophys.* 365, L248-L253, 2001.



Fig. 1. ACIS image of G21.5-0.9 using all available ACIS data (Table 1). Red corresponds to 0.2-1.5 keV, green to 1.5-3.0 keV, and blue to 3.0-10.0 keV. The entire remnant is shown on the top and the 40''-radius plerion is shown on the bottom.

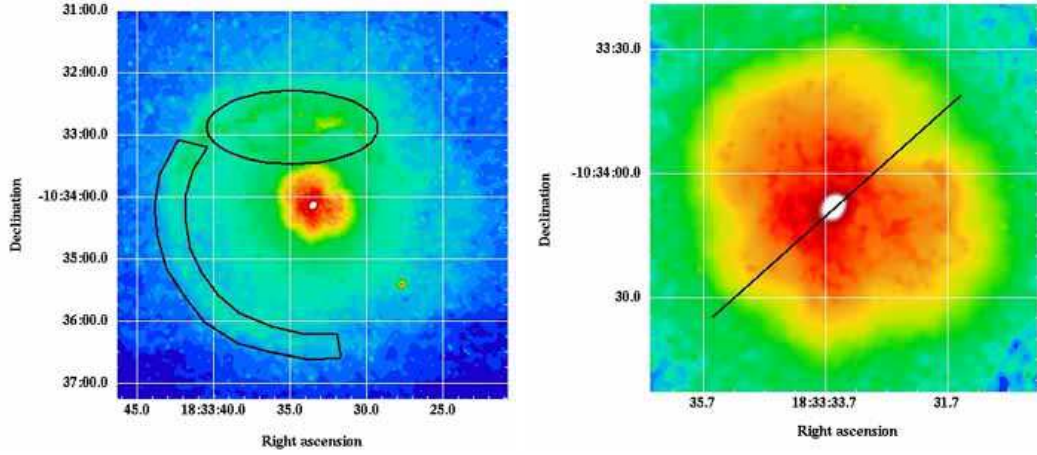


Fig. 2. ACIS images of G21.5-0.9, revealing a faint X-ray halo with limb-brightening in the east. The regions selected for spectral analysis were the northern knots and the eastern limb (see §3). The right image highlights the structure observed in the plerion.

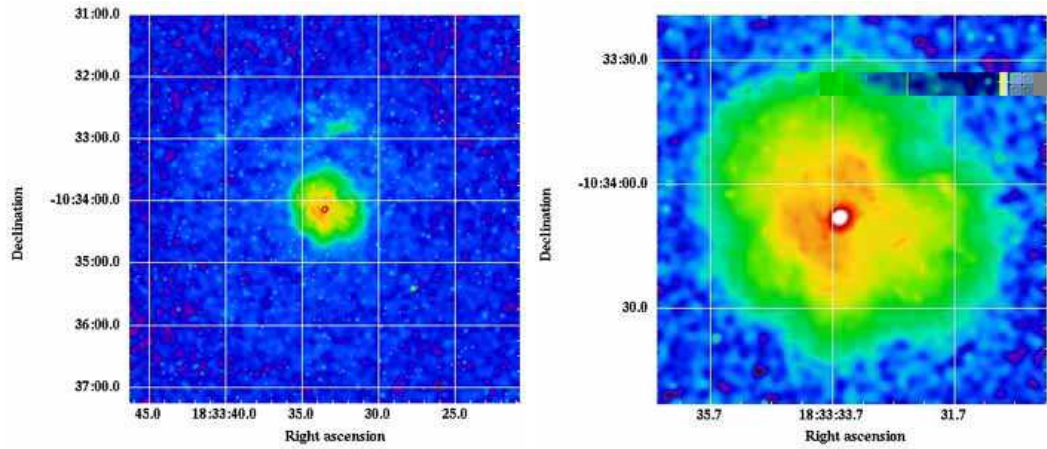


Fig. 3. HRC-I images of G21.5-0.9.

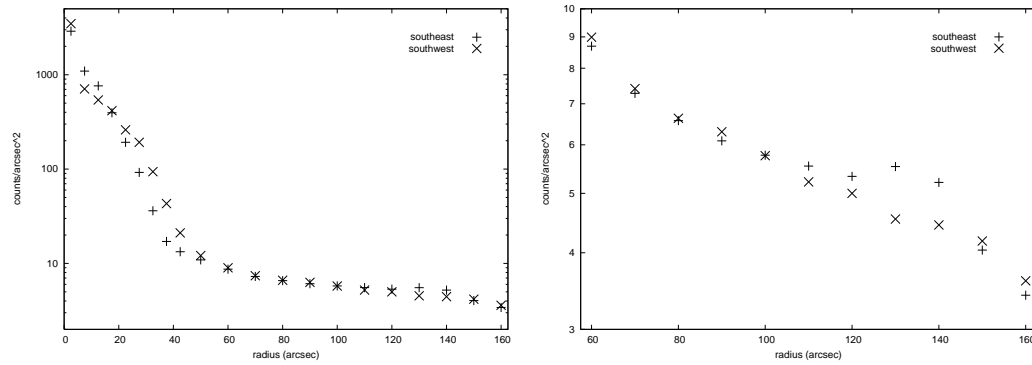


Fig. 4. Radial profiles of the southeast and southwest quadrants of G21.5-0.9. The excess emission seen in the right panel between $\sim 120''$ and $140''$ corresponds to the limb-brightening in the east (see also Fig. 1).

Detector	Time	Observations (off-axis angles)
ACIS-I, -100°C	41.9	158 (5.8'), 160 (6.7'), 161 (5.9'), 162 (1.7')
ACIS-I, -110°C	100.4	1233 (1.7'), 1441 (9.3'), 1442 (5.8'), 1443 (5.9'), 1772 (7.3'), 1773 (5.8'), 1774 (4.3'), 1775 (2.5'), 1776 (0.8'), 1777 (5.8'), 1778 (4.3'), 1779 (2.5')
ACIS-I, -120°C	127.5	1551 (2.5'), 1552 (2.5'), 1719 (7.3'), 1720 (5.8'), 1721 (4.3'), 1722 (2.5'), 1723 (0.8'), 1724 (5.8'), 1725 (4.3'), 1726 (2.5'), 2872 (3.7'), 3473 (7.0'), 3692 (2.5'), 3699 (3.7'), 5165 (3.8')
ACIS-S, -100°C	36.8	159 (0.3'), 165 (6.2'), 1230 (0.3')
ACIS-S, -110°C	68.2	1433 (1.2'), 1434 (6.2'), 1769 (1.3'), 1770 (1.3'), 1771 (1.3'), 1780 (4.7'), 1781 (4.7'), 1782 (4.7')
ACIS-S, -120°C	145.7	1553 (1.3'), 1554 (1.2'), 1716 (1.3'), 1717 (1.3'), 1718 (1.3'), 1727 (4.7'), 1728 (4.6'), 1729 (4.6'), 1838 (1.2'), 1839 (2.4'), 1840 (5.3'), 2873 (1.2'), 3474 (7.0'), 3693 (1.2'), 3700 (1.2'), 4353 (5.2'), 5166 (1.2')
HRC-I	245.2	142 (0.3'), 143 (0.3'), 144 (0.3'), 1242 (0.4'), 1298 (0.3'), 1406 (0.3'), 1555 (0.3'), 1556 (0.3'), 2867 (0.3'), 2874 (0.3'), 3694 (0.3'), 3701 (0.2'), 5167 (0.3')

Table 1

Net exposure times (in ksec) and off-axis angles for *CHANDRA* data.

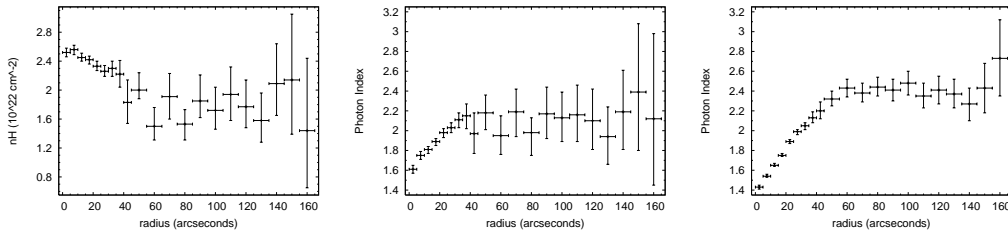


Fig. 5. The variation of N_H and Γ across G21.5-0.9. **Left:** Radial variation of N_H for an absorbed powerlaw. **Centre:** Radial variation of Γ when N_H is allowed to vary freely in an absorbed powerlaw. **Right:** Radial variation of Γ when N_H is frozen at $2.2 \times 10^{22} \text{ cm}^{-2}$ (the best fit value) in an absorbed powerlaw model.

Model	Parameter	northern knots	eastern limb
power	N_H (10^{22} cm $^{-2}$)	1.86 (1.70-2.06)	1.86 (1.37-2.14)
	Γ	2.07 (1.96-2.21)	2.15 (1.81-2.52)
	reduced chi-sq (dof)	1.11 (108)	0.993 (69)
power*	Γ	2.29 (2.24-2.34)	2.37 (2.24-2.50)
	reduced chi-sq (dof)	1.18 (109)	0.995 (70)
<i>pshock</i>	N_H (10^{22} cm $^{-2}$)	1.56 (1.44-1.68)	1.47 (1.11-1.83)
	kT (keV)	4.98 (4.39-5.88)	4.84 (3.39-7.28)
	$n_e t$ (10^8 s cm $^{-3}$)	1 (1-6.28)	1 (1-15.9)
	reduced chi-sq (dof)	1.11 (107)	1.02 (68)
<i>pshock</i> *	kT (keV)	5.22 (4.83-5.77)	4.90 (3.86-7.15)
	$n_e t$ (10^9 s cm $^{-3}$)	9.8 (8.6-11.1)	13.0 (8.4-21.4)
	reduced chi-sq (dof)	1.91 (108)	1.15 (69)

Table 2

Results obtained by fitting ACIS-I, -120°C spectra simultaneously in XSPEC (0.5-8.0 keV, 90% confidence ranges). Fig. 6 and 7 show the powerlaw fits when N_H is allowed to vary. Abundances are consistent with solar for the *pshock* model. * N_H frozen to 2.2×10^{22} cm $^{-2}$.

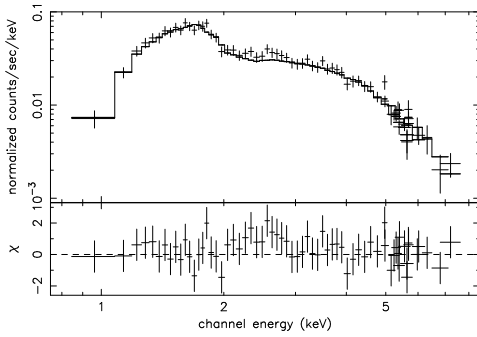


Fig. 6. Absorbed powerlaw fit to the ACIS-I, -120°C data of the northern knots. Excess emission is visible, indicating marginal evidence for sulfur and silicon in the knots.

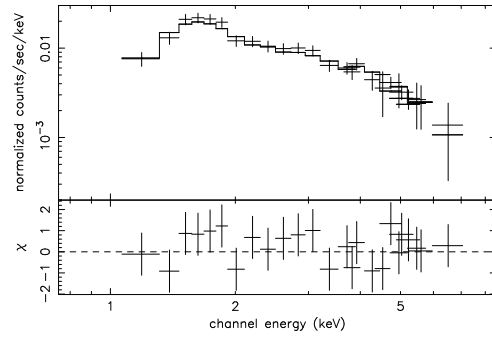


Fig. 7. Absorbed powerlaw fit to the ACIS-I, -120°C data of the eastern out-ermost arc.